Supporting Information

Chemical and structural evolutions of Li-Mn-rich layered electrodes under different current densities

Xin He[a,b,c#], Jue Wu[d,e#], Zhuoying Zhu[b#], Haodong Liu[f], Ning Li[b], Dong Zhou[g], Xu Hou[h], Jun Wang[g], Haowei Zhang[c], Dominic Bresser[i], Yanbao Fu[b], Matthew J Crafton[b,j], Bryan D McCloskey[b,j], Yan Chen[k], Ke An[k], Ping Liu[f], Anubhav Jain[b*], Jie Li[l*], Wanli Yang[d*], Yong Yang[e], Martin Winter[g,h], Robert Kostecki[b*]

a. School of Chemical Engineering at Sichuan University, Chengdu, 610065, China
b. Energy Storage & Distributed Resources Division, Lawrence Berkeley National Laboratory, 1 Cyclotron Road, Berkeley, CA, 94720, USA
c. College of Electrical Engineering at Sichuan University, Chengdu, 610065, China
d. Advanced Light Source, Lawrence Berkeley National Laboratory, Berkeley, California 94720, United States
e. State Key Laboratory for Physical Chemistry of Solid Surfaces, Department of Chemistry, College of Chemistry and Chemical Engineering, Xiamen University, Xiamen 361005, China
f. Department of Nanoengineering, University of California San Diego, La Jolla, CA, 92093, United States
g. MEET Battery Research Center, Institute of Physical Chemistry, University of Münster, Corrensstraße 46, 48149 Münster, Germany
h. Helmholtz Institute Münster – Forschungszentrum Jülich GmbH (IEK 12), Corrensstrasse 46, 48149 Münster, D-48149 Münster, Germany
i. Helmholtz Institute Ulm (HIU), Ulm 89081, Germany
j. Department of Chemical and Biomolecular Engineering, College of Chemistry, University of California, Berkeley, CA, 94720, United States
k. Neutron Scattering Division, Oak Ridge National Laboratory, Oak Ridge, TN, 37830, USA
l. Department of Energy, Politecnico di Milano, Via Lambruschini 4, Milano, 20156, Italy

[#] These authors made equal contributions
* Corresponding author

Experimental

Material synthesis.

The Li-Mn-rich layered oxide $Li_{1.2}Ni_{0.16}Co_{0.08}Mn_{0.56}O_2$ was prepared by a co-precipitation method followed by a high-temperature annealing procedure. $NiSO_4 \cdot 6H_2O$, $CoSO_4 \cdot 7H_2O$, and $MnSO_4 \cdot 4H_2O$ (2:1:7 in molar) were dissolved in distilled water to form a solution. Then, a mix of Li_2CO_3 and NH_4OH solution was pumped into a continuously stirring tank reactor (CSTR) at room temperature. The resulting precipitates were washed several times with distilled water to remove residual Li^+. After being dried in a vacuum oven at 80 ^oC for over 12 h, Stoichiometric amounts of the $(Ni_{0.2}Co_{0.1}Mn_{0.7})CO_3$ precipitate and Li_2CO_3 were thoroughly mixed at a molar ratio of 1:0.55 to form the precursor powders. The precursor was first heated at 500 ^oC for 5h, then calcined at 850 ^oC in the air for 15h, and finally cooled to room temperature, naturally.

Electrochemical measurements.

Electrodes were prepared by casting a slurry with the composition of 80 wt% $Li_{1.2}Ni_{0.16}Co_{0.08}Mn_{0.56}O_2$ active material, 10 wt% Super C65 and 10 wt% PVdF on aluminum foil. After drying under vacuum at 110 °C overnight, the electrode sheet has been punched to ∅ 12 mm discs. The average mass loading of active material was about 2.5 mg cm^{-2}. The electrodes were assembled into two-electrodes T-cells[53] with pre-activated lithium foil as a counter electrode. 100µl 1M $LiPF_6$ in 1:1(wt %) ethylene carbonate (EC): dimethyl carbonate (DMC) was added as electrolyte. The lithium foil was first electro-deposited in a symmetric cell at 0.5 mA cm^{-2} for 2 hours to lower the influence of solid electrolyte interphase (SEI)[54] formation on the lithium electrode. The cells were disassembled after electrochemical test, and electrodes were washed twice by DMC solvent. Then the electrodes were dried at 60°C under vacuum and kept at Ar atmosphere for further measurements.

Synchrotron sXAS and mRIXS measurements.

Soft XAS measurements were carried out on beamline 10-1 at SSRL. Ni, Co, and Mn L-edge spectra were acquired under an ultrahigh vacuum (10^{-9} Torr) in a single load at room temperature using total electron yield (TEY) via the drain current and fluorescence yield (TFY) via Silicon Photodiodes. All the TEY and TFY spectra were normalized to the beam flux measured by the gold mesh. The resolution of the excitation energy was 0.15 eV.

The O *K*-edge sXAS and mRIXS data were collected in the iRIXS endstation at Beamline 8.0.1 of Advanced Light Source (ALS) at Lawrence Berkeley National Laboratory (LBNL).[55] For mRIXS experiments, to avoid air exposure, the cycled cathodes were disassembled and mounted in an Ar-filled glove box. The samples were transferred to the experimental vacuum chamber via a homemade sample transfer kit to avoid any air exposure. All data were collected from the side of the electrodes facing the current collector by cleaving the electrode. The lowest possible incident beam flux was used with samples keep moving to eliminate the possible irradiation effect and to collect the signals over a large area of electrodes. The mRIXS maps were obtained after energy calibration and normalization to collection time and incident X-ray beam flux, through a multi-step data process.

mRIXS -sPFY data. The O *K*-edge mRIXS-sPFY profiles were obtained via integrating the mRIXS intensity in the range of emission energy from 523 to 524 eV, where the oxidized-oxygen feature appeared. In order to quantify the oxidized-oxygen feature, the area of the mRIXS-sPFY feature was measured (Table S1) by integrating the peak area from 530 to 532 eV excitation energy, with a peak intensity normalization at 529.8 eV excitation energy. Details and demonstrations of this analysis have been reported previously[24]**.**

Neutron diffraction. Time of flight (TOF) powder neutron diffraction data was collected at the VULCAN instrument at the Spallation Neutron Source (SNS), Oak Ridge National Laboratory.[56] At VULCAN, approximately 1.6g of the powder sample was loaded into a vanadium sample can of 6mm diameter in a helium-filled glove box. An incident beam (5 mm × 12 mm) of 0.7 to 3.5 Å bandwidth, allowing 0.5~2.5

Å d-space in the diffracted pattern of the ±90◦ 2θ detector banks, was selected using the double-disk choppers at 30 Hz frequency. The high-resolution mode was employed with delta d/d ~0.25%. The SNS was at nominal, 1400 kW, power. Powder neutron diffraction data were collected in the high-resolution mode for a duration of 3 h and processed using VDRIVE software. The data were normalized to a vanadium rod. Rietveld refinement of the neutron diffraction data was performed using GSAS software with EXPGUI interface.[57,58]

Operando DEMS.

The Operando DEMS experiment was carried out in a sealed electrochemical cell. The positive electrodes were prepared with mass of around 8 mg. The assembled cell was electrochemical controlled by Land CT 2001A battery testers in room temperature. During the measurement, high-purity argon gas flowed through the main chamber of the cell as the carrier gas and were detected using the quadrupole mass spectrometer (Hiden Analytical), the flow rate was controlled at 0.6 mL min-1 using a digital mass flow meter. The detected CO2 and O2 were quantified via the known amounts of reference gases.

Calculation details.

All DFT[59] calculations were performed using the Vienna ab initio simulation package (VASP)[60]with the projector augmented wave (PAW) method[61]. The Perdew–Burke–Ernzerhof (PBE) generalized gradient approximation (GGA) functional[62] with a Hubbard *U* extension of 3.9 eV for manganese, 3.32 eV for cobalt and 6.2 eV for nickel was adopted for structural relaxations and energy calculations[63,64]. All calculations were initialized in a ferromagnetic high-spin configuration because the energy affected by antiferromagnetic ordering is very small (< 3 meV/atom) based on our calculations. A plane wave energy cutoff of 520 eV and k-point density of at least 1,000/*n*, where *n* is the number of atoms in the unit cell, was used for initial relaxations. These settings are consistent with those used for the Materials Project[65]. The energies and forces were converged to 10^{-5} eV per cell and 0.05 eV $Å^{-1}$, respectively.

Structure enumeration and relaxation

To prepare the pristine structure of $Li_{1.2}Ni_{0.16}Co_{0.08}Mn_{0.56}O_2$, a 3 × 2 × 2 supercell of the $Li_{1+\alpha}M_{1-\alpha}O_2$ (M=Ni, Mn, Co) primitive cell (space group: R-3m) was created, which is 12 formula units of $Li_{1+\alpha}M_{1-\alpha}O_2$. In the transition metal layer, the occupancy of cations was set as Li: Ni: Co: Mn = 2:2:1:7, whereas the Li layer was fully occupied by 12 Li atoms (with supercell formula $Li_{14}Ni_2CoMn_7O_{24}$). All symmetrically distinct *TM* layer orderings were generated by the enumlib[66] package in Python Materials Genomics (pymatgen)[67]. Due to the large number of cation orderings (>1000), we applied the MatErials Graph Network (MEGNET[49]) deep learning model to screen out low-energy configurations.[68] A group of 100 random structures with distinct cation arrangements were used for the DFT-energy vs. MEGNET-energy parity plot after structural relaxations (Figure S11). Then the low-energy configurations (E_{hull} < 5 meV/atom) were relaxed with the PBE+*U* functional to obtain the ground-state pristine Li-rich NCM structure for the following calculations.

The initial charge-discharge cycle with different rates (10C vs. 0.1C) leads to two delithiated phases based on the amount of O_2 (0% vs. 4%) released from the pristine Li-rich NCM. The Li content was fixed to x~0.83 for DFT calculations, where O_2 started to be released at 4.42V-4.8V plateau region under 0.1C[46]. To obtain this composition of $Li_{10}Ni_2CoMn_7O_{24}$ ($Li_{8/12}[Li_{2/12}Ni_{2/12}Co_{1/12}Mn_{7/12}]O_2$), we extracted 4/12 Li ions in the Li layer from the ground-state $Li_{14}Ni_2CoMn_7O_{24}$ ($Li[Li_{2/12}Ni_{2/12}Co_{1/12}Mn_{7/12}]O_2$) structure (see **Figure 5**). The other Li ions in the TM layers remain in their positions which matches with the experimental refinement results in Table S5, S6. Different Li orderings in $Li_{10}Ni_2CoMn_7O_{24}$ ($Li_{8/12}[Li_{2/12}Ni_{2/12}Co_{1/12}Mn_{7/12}]O_2$) were fully relaxed and the lowest-energy configuration was used for the following oxygen vacancy generation and NEB calculations.

To mimic 4% oxygen vacancy in $Li_{0.83}Ni_{0.16}Co_{0.08}Mn_{0.56}O_{1.92}$ after 0.1C charge-discharge cycle, we sequentially extracted 2/48 oxygen atoms in a 3 × 4 × 2 supercell, leading to the formula of $Li_{20}Ni_4Mn_{14}Co_2O_{46}$ ($Li_{8/12}[Li_{2/12}Ni_{2/12}Co_{1/12}Mn_{7/12}]O_{23/12}$). After removing the first oxygen atom, we found the energy is highly dependent on the local environments of oxygen vacancy, to be more specific, the nearest coordinated *TM* metals in the *TM* layer (see **Figure 6**). The electrostatic repulsion between oxygen vacancy and *TM* are increasing by order of Ni < Co < Mn.

NEB calculations

Climbing-image nudged elastic band (CI-NEB)[69]calculations were performed using 3 × 4 × 2 supercells of the Li*M*O_2 primitive cell. The supercell choice was applied to maximize the distance between periodic images of the paths and to match with 4% oxygen vacancy concentration as observed in the experiments. For all the NEB calculations, five linearly interpolated intermediate images of the initial guess were adopted with the energies and forces convergences of 10^{-5} eV per supercell and 0.02 eV $Å^{-1}$, respectively.

For 10C rate without oxygen vacancy, the supercell has a formula of $Li_{20}Ni_4Co_2Mn_{14}O_{48}$ (unit cell formula: $Li_{8/12}[Li_{2/12}Ni_{2/12}Co_{1/12}Mn_{7/12}]O_2$), which is roughly equivalent to $Li_{0.83}Ni_{0.16}Co_{0.08}Mn_{0.56}O_2$. We used the lowest-energy configuration from cation orderings and performed the Li vacancy *o-t-o* hops categorized by the intermediate tetrahedral site because only the local atomic arrangements, especially the face-sharing *TM*, have a substantial effect on the migration barriers[52]. The barriers for 3 symmetrically distinct paths were computed (see Figure S12 (a-c)) when the face-sharing TM is Ni, Co and Mn.

For 0.1C with 4% oxygen vacancy, the supercells we used have a formula of $Li_{20}Ni_4Co_2Mn_{14}O_{46}$ (unit cell formula: $Li_{8/12}[Li_{2/12}Ni_{2/12}Co_{1/12}Mn_{7/12}]O_{23/12}$), which is roughly equivalent to $Li_{0.83}Ni_{0.16}Co_{0.08}Mn_{0.56}O_{1.92}$. Two configurations with divacancy distances of 5.8Å (the ground-state configuration) and 3.1Å (9 meV/atom higher in energy than the ground state) were chosen to perform the *o-t-o* hops. 5 distinct paths were computed as shown in Figure S12 (d-f). The migration barriers are affected by many factors like *TM* species, the local environments of the oxygen vacancy (primary or secondary for the paths), and divacancy distances. The strong repulsion between divacancies makes it unlikely to have two vacancies within the same TMO_6 octahedron. The minimum divacancy distance we found with a reasonably low configuration

energy is ~3.1Å. And this intensive local oxygen vacancy does help to reduce the migration barriers furthermore (see Figure S12 (d)).

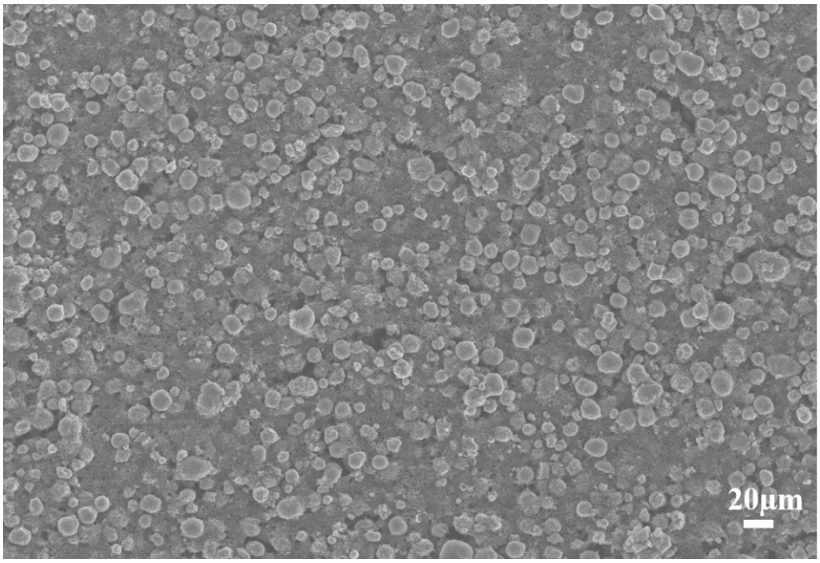

Figure S1. SEM image of the prepared electrode with LMR-NCM material

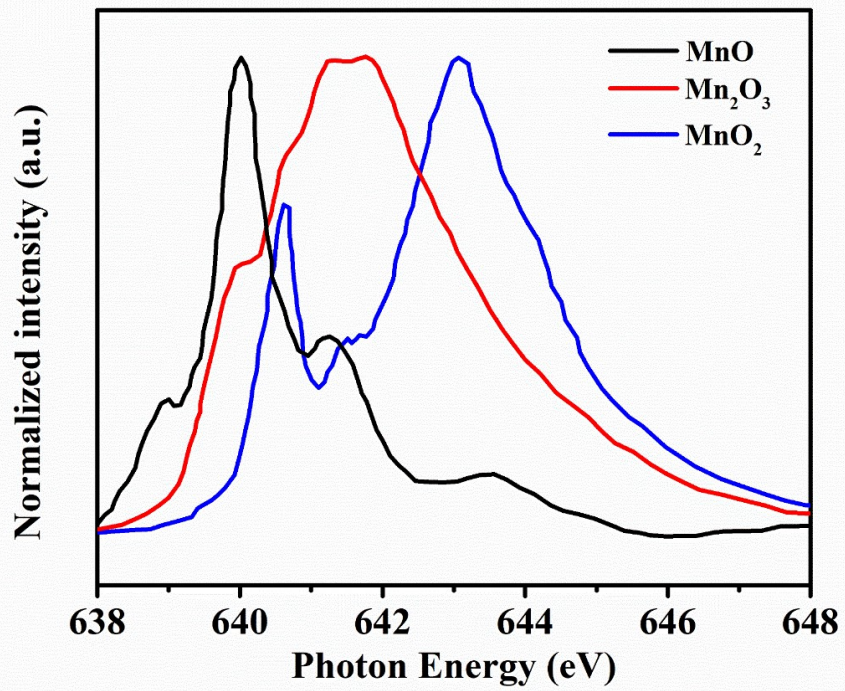

Figure S2. Mn *L*-edge sXAS spectra for MnO, Mn_2O_3, and MnO_2 as reference spectra for Mn^{2+}, Mn^{3+}, and Mn^{4+} ions, respectively.

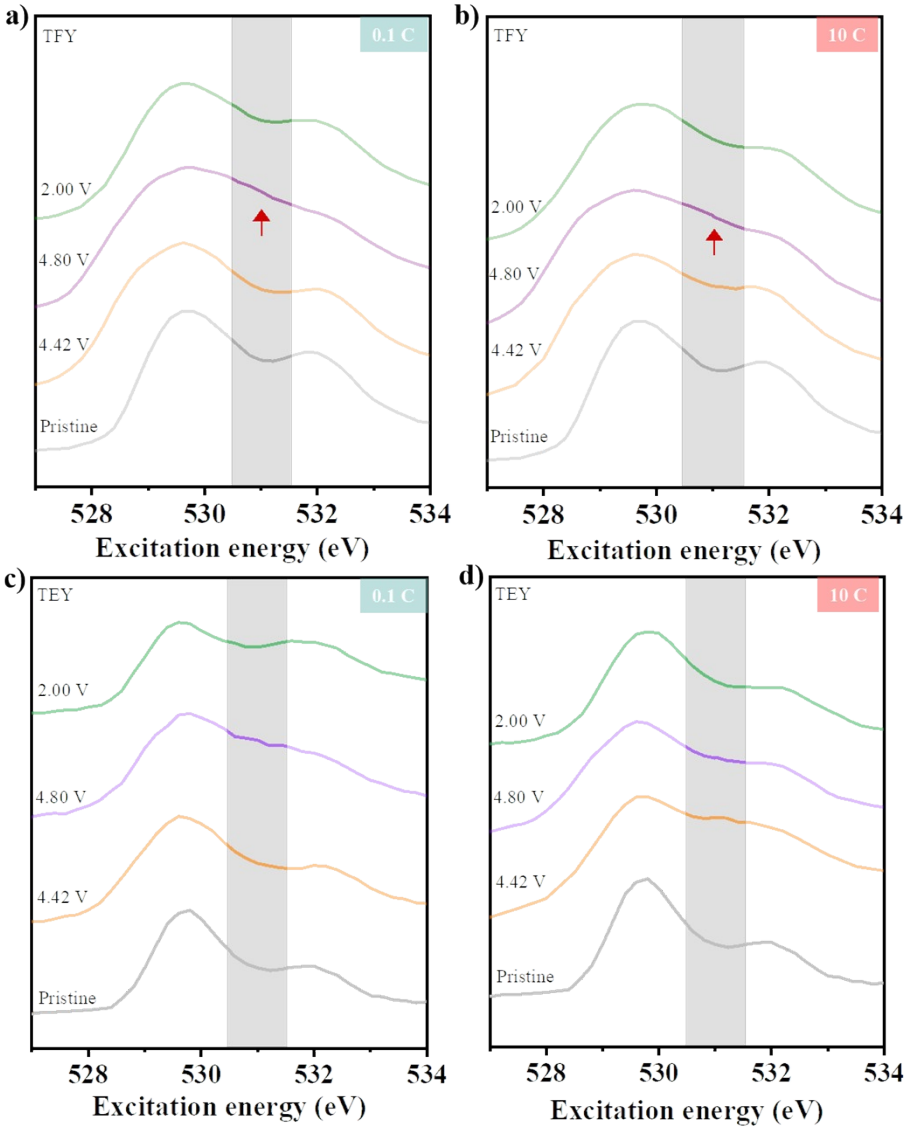

Figure S3. O K-edge sXAS spectra for Li-rich electrodes at different SOCs in TFY and TEY modes.

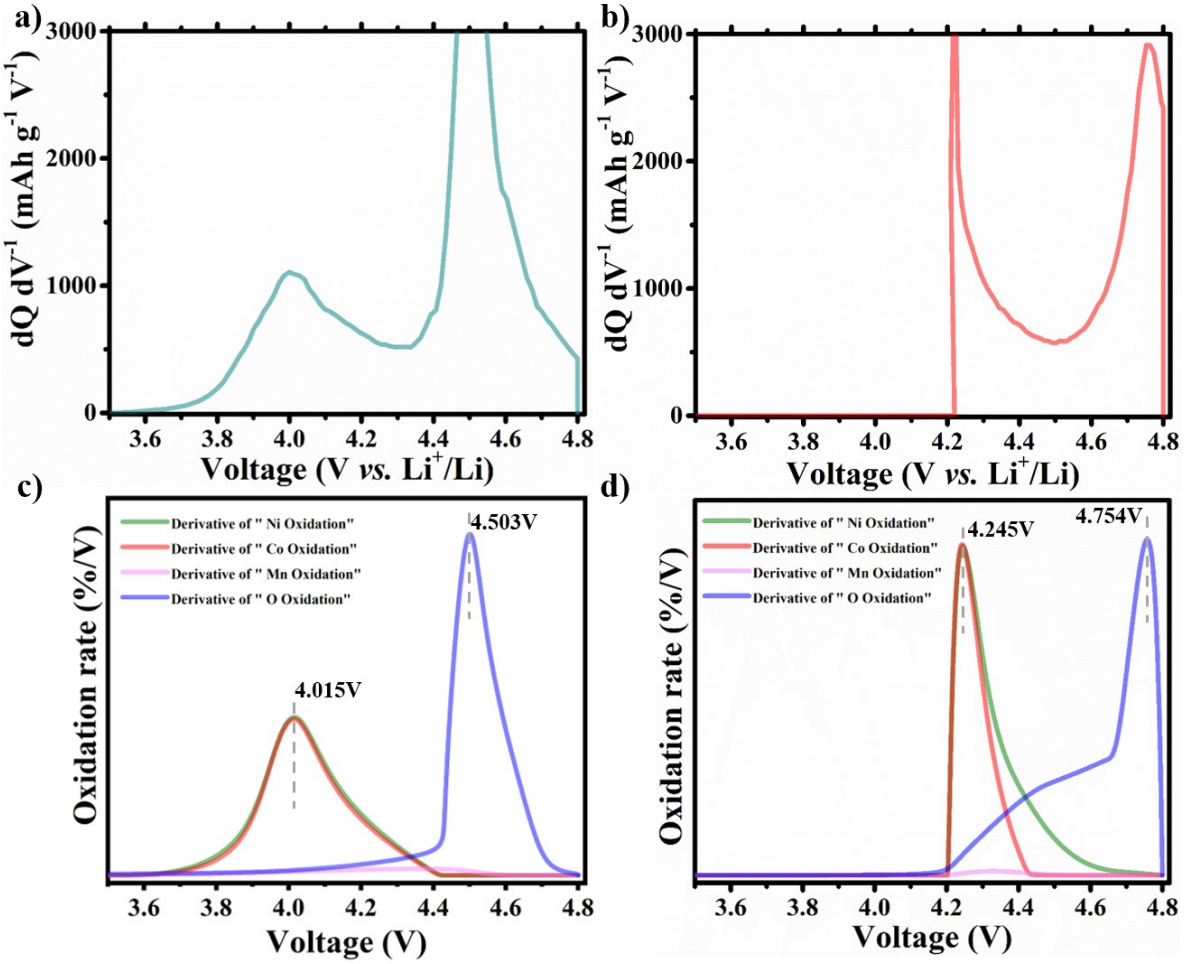

Figure S4. dQ/dV vs. voltage plots of the first charge processes at 0.1C (a) and 10C (b), and the simulation of corresponding active Li-rich materials charge compensation mechanism based on the mean valence state of involved elements.

Table S1. Peak area evolutions and corresponding delivered capacities at 0.1C and 10C

Cycle	Rate	Sample	sPFY area (a.u.)	Area change (a.u.)	Reversibility of area change	Capacity (mAh/g)	Coulombic efficiency (%)
1st		**Pristine**	0.01367	0.0000	--	--	--
	0.1C	**0.1C-4.42 V**	0.01465	0.00098	Discharge/charge: (0.01028-0.00129)/0.01028 =87.5%	102.8	92.8%
		0.1C-4.80 V	0.02395	0.01028		300.2	
		0.1C-2.00 V	0.01496	0.00129		278.4	
	10C	**10C-4.42 V**	0.01571	0.00204	Discharge/charge: (0.00945-0.00315)/0.00945 =66.7%	50.6	65.6%
		10C-4.6 V	0.01658	0.00291			
		10C-4.80 V	0.02312	0.00945		156.6	
		10C-2.00 V	0.01682	0.00315		102.7	

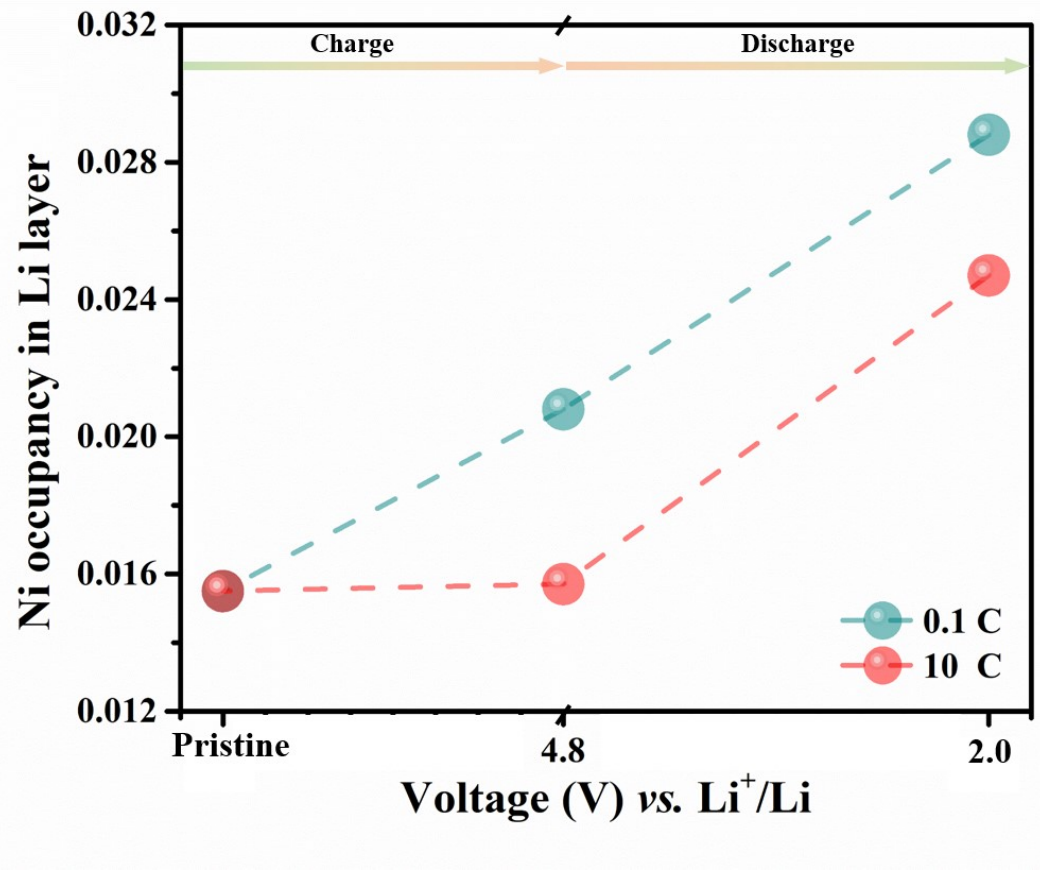

Figure S5. Refinement results of Ni occupancy in Li layer at different states with the current rates of 0.1C and 10C, respectively.

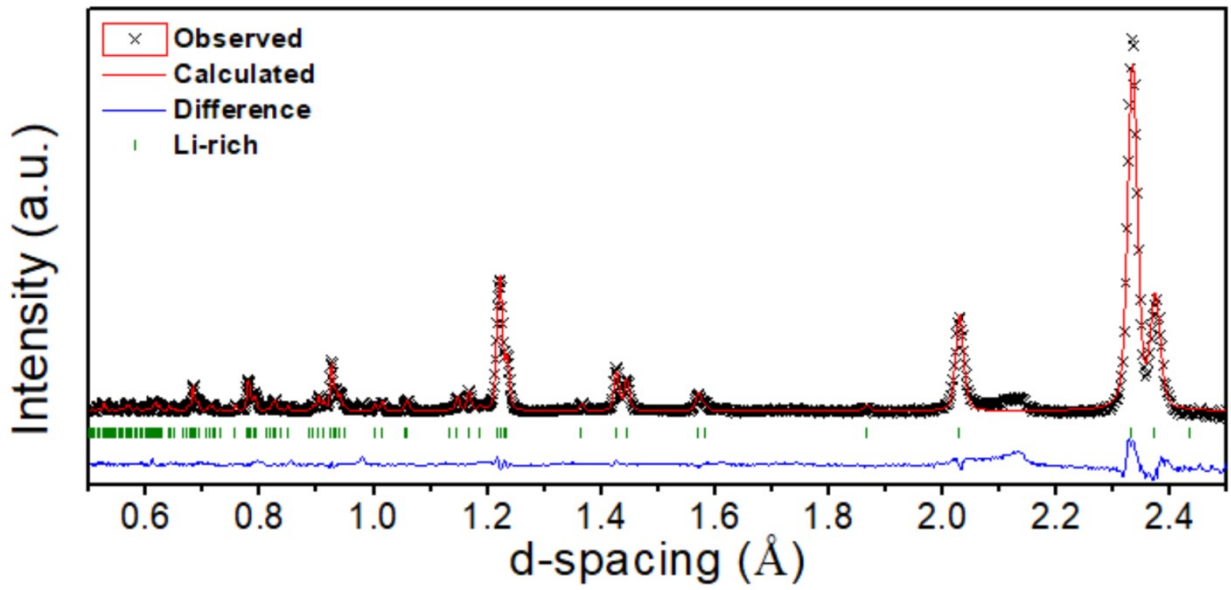

Figure S6. Refined neutron powder diffraction pattern of Li-rich material at the open circuit potential state.

Table S2. Refinement results of the Li-rich material at the open circuit voltage (OCV) state.

Space group: R-3m, R_{wp} = 4.52% **a = b = 2.8501(2) Å, c = 14.232(1) Å, α=β=90°, γ=120°**				
Atoms	Wyckoff positions			Occupancy
Li	0	0	0.5	0.215(5)
Ni	0	0	0.5	0.145(5)
Mn	0	0	0.5	0.56
Co	0	0	0.5	0.08
O	0	0	0.2412(1)	1
Li	0	0	0	0.985(5)
Ni	0	0	0	0.015(5)

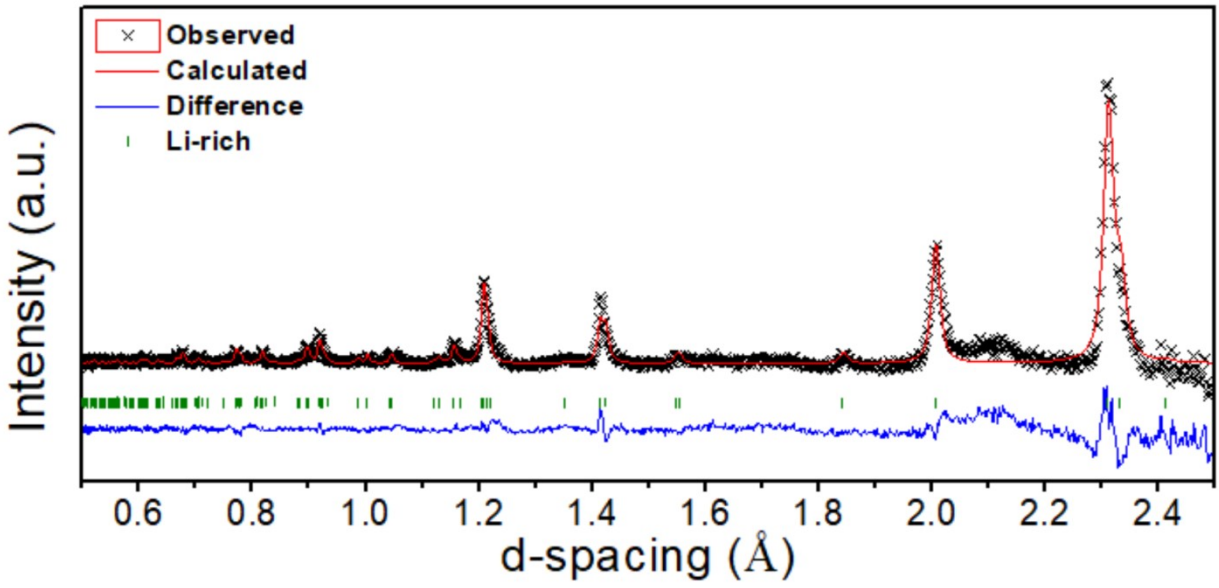

Figure S7. Refined neutron powder diffraction pattern of fully charged Li-rich material (4.8V) at 0.1C

Table S3. Refinement results of the of fully charged Li-rich material (4.8V) at 0.1C

Space group: R-3m, R_{wp} = 2.70% **a = b = 2.8259(6) Å, c = 13.990(4) Å, α=β=90°, γ=120°**				
Atoms	Wyckoff positions			Occupancy
Li	0	0	0.5	0.069(8)
Ni	0	0	0.5	0.140(8)
Mn	0	0	0.5	0.56
Co	0	0	0.5	0.08
O	0	0	0.2373(2)	0.961(9)
Li	0	0	0	0.178(8)
Ni	0	0	0	0.020(8)

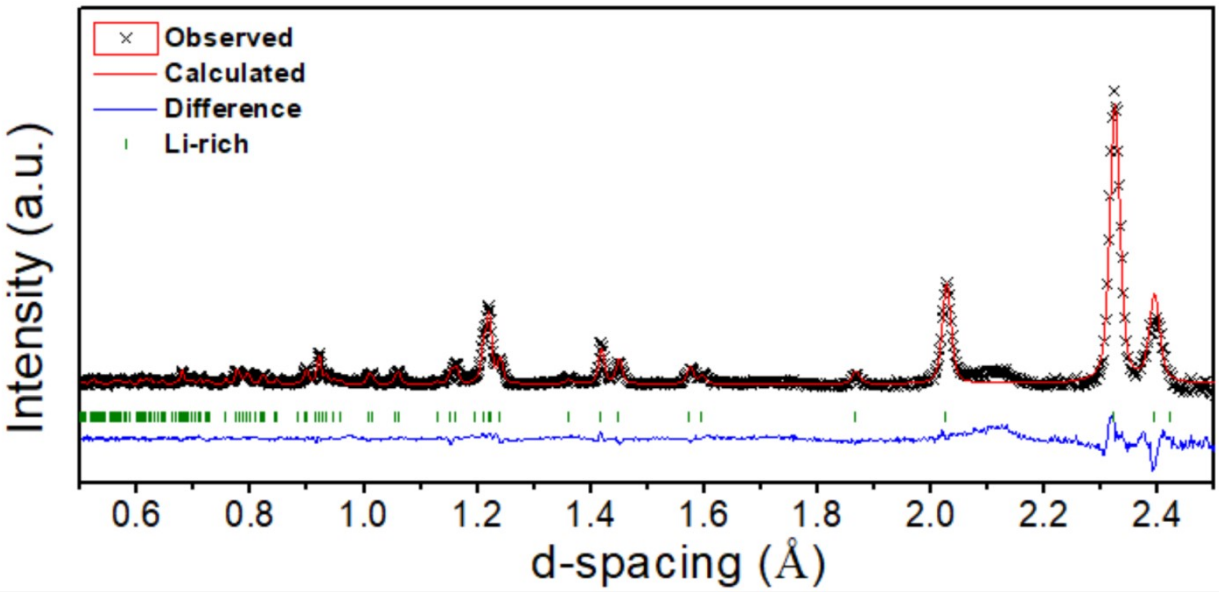

Figure S8. Refined neutron powder diffraction pattern of fully charged Li-rich material (4.8V) at 10C

Table S4. Refinement results of the of fully charged Li-rich material (4.8V) at 10C

Space group: R-3m, R_{wp} = 3.09% **a = b = 2.8345(3) Å, c = 14.354(2) Å, α=β=90°, γ=120°**				
Atoms	Wyckoff positions			Occupancy
Li	0	0	0.5	0.141(3)
Ni	0	0	0.5	0.146(3)
Mn	0	0	0.5	0.56
Co	0	0	0.5	0.08
O	0	0	0.2386(1)	0.996(9)
Li	0	0	0	0.520(3)
Ni	0	0	0	0.015(7)

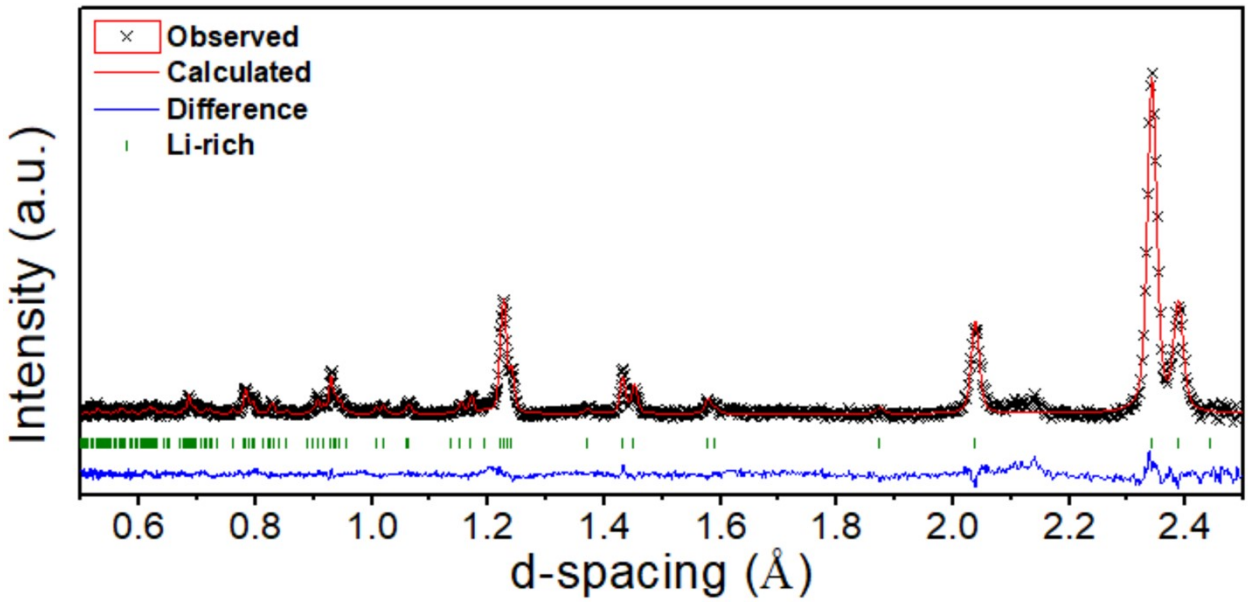

Figure S9. Refined neutron powder diffraction pattern of fully discharged Li-rich material (2V) at 0.1C

Table S5. Refinement results of the of fully discharged Li-rich material (2V) at 0.1C

Space group: R-3m, R_{wp} = 2.48% **a = b = 2.8599(3) Å, c = 14.316(2) Å, α=β=90°, γ=120°**				
Atoms	Wyckoff positions			Occupancy
Li	0	0	0.5	0.181(8)
Ni	0	0	0.5	0.132(8)
Mn	0	0	0.5	0.56
Co	0	0	0.5	0.08
O	0	0	0.2411(1)	0.961(9)
Li	0	0	0	0.949(8)
Ni	0	0	0	0.028(8)

Figure S10. Refined neutron powder diffraction pattern of fully discharged Li-rich material (2V) at 10C

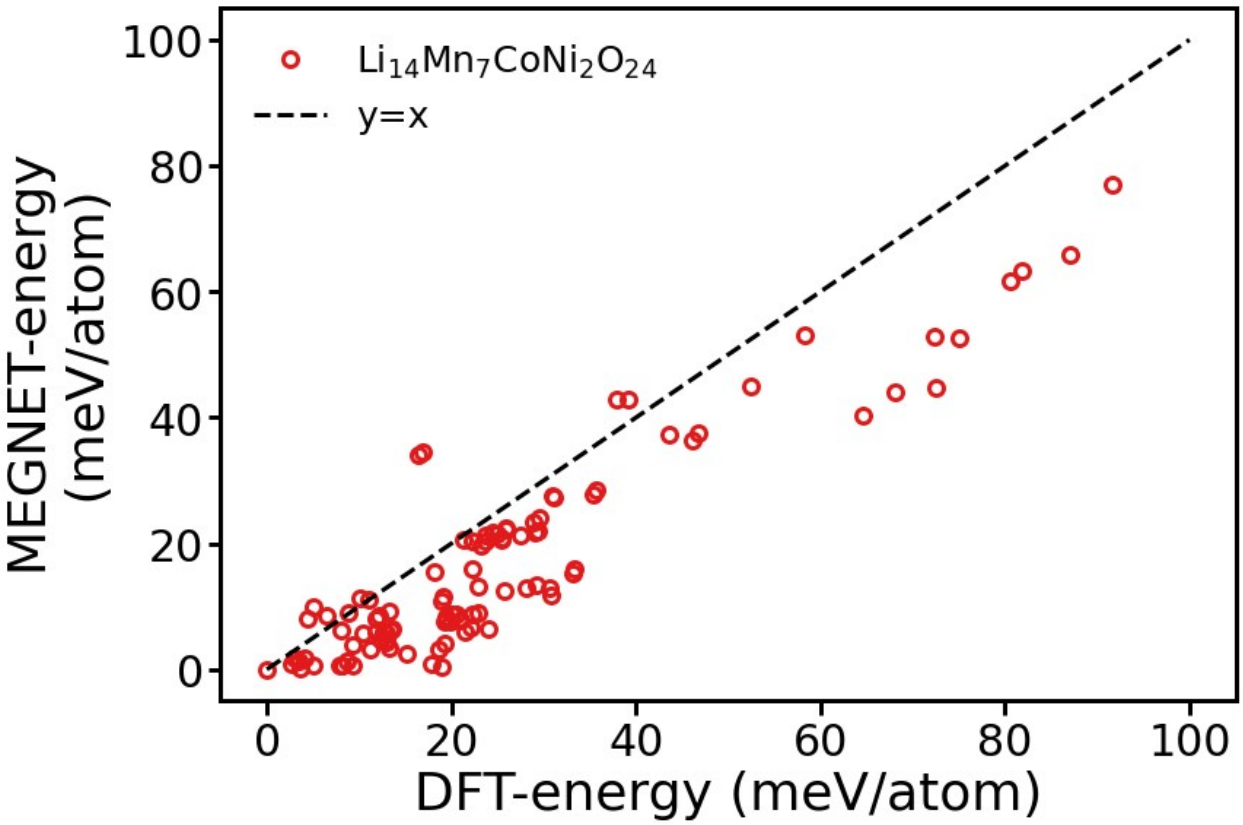

Figure S11. Parity plot of DFT-energy and MEGNET predicted energy of 100 randomly selected structures of $Li_{14}Ni_2CoMn_7O_{24}$ with different cation orderings.

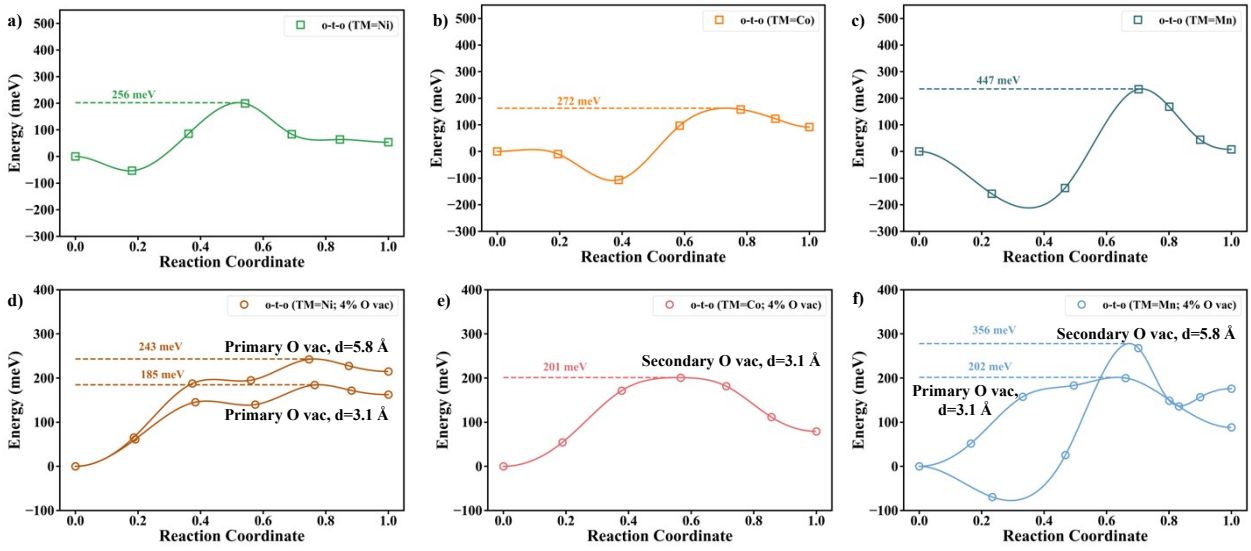

Figure S12. NEB barriers of $Li_{0.83}Ni_{0.16}Mn_{0.56}Co_{0.08}O_2$ at 10C (**a-c**) and $Li_{0.83}Ni_{0.16}Mn_{0.56}Co_{0.08}O_{1.92}$ at 0.1C (**d-f**). Panels (**a-c**) refer to the *o-t-o* migration barriers when tet site is face-sharing with a TM (TM=Ni, Co, Mn) without oxygen vacancy in the lattice. At 10C, the *o-t-o* migration barriers are ranging from 256 meV (TM=Ni) to 447 meV (TM=Mn). Panels (**d-f**) refer to the *o-t-o* migration barriers with 4% oxygen vacancy at 0.1C. The values are greatly decreased from 10C, showing the

migration barriers as low as 185 meV (TM=Ni), 201 meV (TM=Co) and 202 meV (TM=Mn). Two configurations with different divacancy distances (d=3.1Å or d=5.8Å) are applied for the NEB calculations. The primary O vacancy indicates the position of oxygen vacancy (either in the oct vertex of LiO_6 or the tet vertex of intermediate LiO_4 in the *o-t-o* path as shown in Figure 7). The secondary O vacancy represents the other possible positions.

Table S6. Refinement results of the of fully discharged Li-rich material (2V) at 10C

Space group: R-3m, R_{wp} = 2.37% **a = b = 2.8490(3) Å, c = 14.311(2) Å, α=β=90°, γ=120°**				
Atoms	Wyckoff positions			Occupancy
Li	0	0	0.5	0.170(7)
Ni	0	0	0.5	0.136(7)
Mn	0	0	0.5	0.56
Co	0	0	0.5	0.08
O	0	0	0.2399(1)	0.996(9)
Li	0	0	0	0.852(7)
Ni	0	0	0	0.024(7)

Table S7 tRatio of Li vacancy in Li layer and Li vacancy in transition metal layer

0.1C			10C			
4.42V	4.8V	2.0V	4.42V	4.65V	4.8V	2.0V
25:0	62:10	3:3	13:2	21:4	35:7	10:4

References:

53 R. Nölle, K. Beltrop, F. Holtstiege, J. Kasnatscheew, T. Placke and M. Winter, *Mater. Today*, 2020, **32**, 131–146.

54 H. Liu, H. Liu, I. D. Seymour, N. Chernova, K. M. Wiaderek, N. M. Trease, S. Hy, Y. Chen, K. An, Z. Liu, P. J. Chupas, K. W. Chapman, M. S. Whittingham, P. Grey and Y. Shirley, *J. Mater. Chem. A*, 2018, **6**, 4189–4198.

55 R. Qiao, Q. Li, Z. Zhuo, S. Sallis, O. Fuchs, M. Blum, L. Weinhardt, J. Pepper, M. Jones, A. Brown, A. Spucces, K. Chow, F. Pan, L. F. J. Piper, P. Glans, Y. Chen, S. Yan, M. Blum, L. Weinhardt, C. Heske, J. Pepper, M. Jones, A. Brown, A. Spucces, K. Chow, B. Smith, P. Glans, Y. Chen, S. Yan, F. Pan, L. F. J. Piper and J. Denlinger, *Rev. Sci. Instrum.*, 2017, **88**, 033106.

56 K. E. An, H. D. Skorpenske, A. D. Stoica, D. Ma, X. Wang and E. Cakmak, *Metall. Mater. Trans. A*, 2011, **42A**, 95–99.

57 B. H. Toby, *J. Appl. Crystallogr.*, 2001, **34**, 210–213.

58 A. C. Larson and R. B. V. Dreele, *Los Alamos Natl. Lab. Rep.*, 2004, 86–748.

59 W. Kohn and L. J. Sham, *Phys. Rev.*, 1965, **140**, A1133–A1138.

60 G. Kresse and J. Furthmueller, *Phys. Rev. B*, 1995, **54**, 11169–11186.

61 P. E. Blöchl, *Phys. Rev. B*, 1994, **50**, 17953–17979.

62 J. P. Perdew, K. Burke and M. Ernzerhof, *Phys. Rev. Lett.*, 1996, **77**, 3865–3868.

63 A. K. Padhi, K. S. Nanjundaswamy and J. B. Goodenough, *J. Electrochem. Soc.*, 1997, **144**, 1188–1194.

64 a. I. Lichtenstein, V. I. Anisimov and J. Zaanen, *Phys. Rev. B*, 1995, **52**, 5467–5471.

65 A. Jain, S. P. Ong, G. Hautier, W. Chen, W. D. Richards, S. Dacek, S. Cholia, D. Gunter, D. Skinner, G. Ceder and K. A. Persson, *APL Mater.*, 2013, **1**, 1–11.

66 G. L. W. Hart and R. W. Forcade, *Phys. Rev. B - Condens. Matter Mater. Phys.*, 2008, **77**, 1–12.

67 S. P. Ong, W. D. Richards, A. Jain, G. Hautier, M. Kocher, S. Cholia, D. Gunter, V. L. Chevrier, K. A. Persson and G. Ceder, *Comput. Mater. Sci.*, 2013, **68**, 314–319.

68 L. Yang, C. Chen, S. Xiong, C. Zheng, P. Liu, Y. Ma, W. Xu, Y. Tang, S. P. Ong and H. Chen, *JACS Au*, 2021, **1**, 98–107.

69 G. Henkelman and H. Jónsson, *J. Chem. Phys.*, 2000, **113**, 9978–9985.